

## Communication

**Operando monitoring of the solution-mediated discharge and charge processes in a Na-O<sub>2</sub> battery using liquid-electrochemical TEM**

Lukas Lutz, Walid Dachraoui, Arnaud Demortiere, Lee R. Johnson,  
Peter G. Bruce, Alexis Grimaud, and Jean-Marie Tarascon

*Nano Lett.*, **Just Accepted Manuscript** • Publication Date (Web): 22 Jan 2018

Downloaded from <http://pubs.acs.org> on January 22, 2018

**Just Accepted**

“Just Accepted” manuscripts have been peer-reviewed and accepted for publication. They are posted online prior to technical editing, formatting for publication and author proofing. The American Chemical Society provides “Just Accepted” as a free service to the research community to expedite the dissemination of scientific material as soon as possible after acceptance. “Just Accepted” manuscripts appear in full in PDF format accompanied by an HTML abstract. “Just Accepted” manuscripts have been fully peer reviewed, but should not be considered the official version of record. They are accessible to all readers and citable by the Digital Object Identifier (DOI®). “Just Accepted” is an optional service offered to authors. Therefore, the “Just Accepted” Web site may not include all articles that will be published in the journal. After a manuscript is technically edited and formatted, it will be removed from the “Just Accepted” Web site and published as an ASAP article. Note that technical editing may introduce minor changes to the manuscript text and/or graphics which could affect content, and all legal disclaimers and ethical guidelines that apply to the journal pertain. ACS cannot be held responsible for errors or consequences arising from the use of information contained in these “Just Accepted” manuscripts.



1  
2  
3 1 ***Operando* monitoring of the solution-mediated discharge and charge processes**  
4  
5 2 **in a Na-O<sub>2</sub> battery using liquid-electrochemical TEM**

6  
7 3 Lukas Lutz<sup>1,3,4</sup>, Walid Dachraoui<sup>2,3</sup>, Arnaud Demortière<sup>2,3\*</sup>, Lee R. Johnson<sup>4</sup>,  
8  
9 4 Peter G. Bruce<sup>4</sup>, Alexis Grimaud<sup>1,3\*</sup>, and Jean-Marie Tarascon<sup>1,3</sup>

10  
11  
12 5  
13 6 <sup>1</sup>Collège de France, 11 Place Marcelin Berthelot, 75231 Paris, France

14  
15 7 <sup>2</sup>Laboratoire de Réactivité et Chimie des Solides (LRCS), CNRS UMR 7314, 80009 Amiens, France

16  
17 8 <sup>3</sup>Réseau sur le Stockage Electrochimique de l'Energie (RS2E), FR CNRS 3459, France

18  
19 9 <sup>4</sup>Department of Materials, University of Oxford, Parks Road, Oxford OX1 3PH, UK

20  
21 10  
22  
23 11 Corresponding authors: Alexis Grimaud <alexis.grimaud@college-de-france.fr>,  
24  
25 12 Arnaud Demortière <arnaud.demortiere@energie-rs2e.com>



## 50 **Introduction**

51 Compared to Li/Na-ion batteries, in which reversible energy storage relies on the use of redox  
52 active transition metal oxides as positive electrodes, the metal-O<sub>2</sub> battery systems would  
53 theoretically offer greater energy density owing to the use the redox of gaseous oxygen using  
54 conductive and light carbon electrodes.<sup>1, 2</sup> The aprotic lithium-oxygen (Li-O<sub>2</sub>) system has  
55 been widely studied since the early demonstration of reversibility by K.M. Abraham.<sup>3</sup>  
56 Nevertheless, recent developments clearly pointed out towards drastic limitations in terms of  
57 round trip efficiency as well as coulombic efficiency due to copious parasitic reactions of the  
58 discharge product lithium peroxide (Li<sub>2</sub>O<sub>2</sub>) with both the conductive electrode and the  
59 electrolyte.<sup>4-6</sup> Following this conclusion, the sodium-oxygen (Na-O<sub>2</sub>) system was then  
60 proposed as a viable alternative due to its theoretical energy density of 1100 Wh/kg combined  
61 with a better round trip efficiency and presumably limited parasitic reactions.<sup>7</sup> The Na-O<sub>2</sub>  
62 system is still, however, in its infancy, owing to several unresolved challenges, such as  
63 limited capacities and low cyclability.<sup>8, 9</sup> Hence, the initial excitement was quickly  
64 counterpoised by the recent discoveries highlighting the unstable nature of the superoxide  
65 discharge product sodium superoxide (NaO<sub>2</sub>) that reacts with glyme-ethers solvent commonly  
66 used in these systems. Despite these evident limitations, this system has been seen as an  
67 interesting case study to better understand the complex redox reaction of oxygen in aprotic  
68 solvent that involves a gas to solid phase transformation. Only mastering these complex  
69 transformations will eventually trigger the development of rechargeable metal-O<sub>2</sub> batteries  
70 and deliver the initial promises offered by the large energy density for these systems.

71 Further efforts are thus required to understand and master the formation and decomposition  
72 processes of the micron-sized cubic NaO<sub>2</sub> product, which is at the core of the Na-O<sub>2</sub>  
73 electrochemistry and still under heavy debate. Contradictory results discussing either a  
74 solution-mediated discharge and charge reaction, the need for phase transfer catalysts (e.g.:

1  
2  
3 75 H<sub>2</sub>O) that increases the solubility of NaO<sub>2</sub>, or an electrode-surface directed mechanism, leave  
4  
5 76 the question for the fundamental reaction path unanswered.<sup>5, 10-17</sup> One reason for that is surely  
6  
7 77 the high sensitivity of the NaO<sub>2</sub> product and its reactivity towards moisture<sup>18, 19</sup>, CO<sub>2</sub><sup>20, 21</sup> and  
8  
9 78 other electrolyte impurities, which makes any analysis by *ex situ* methods extremely difficult.  
10  
11 79 This also explains the absence of a common consensus regarding the parameters controlling  
12  
13 80 the formation of NaO<sub>2</sub> as well as the underpinning mechanism for NaO<sub>2</sub> decomposition.<sup>5, 10-17</sup>  
14  
15

16 81 Another challenge of the Na-O<sub>2</sub> system is associated to its unsatisfactory cyclability, where  
17  
18 82 recent papers have demonstrated that the fast death of the battery, after only few cycles, is  
19  
20 83 associated to the low stability of the NaO<sub>2</sub> discharge product.<sup>8, 22</sup> Others further identified the  
21  
22 84 detrimental ability of NaO<sub>2</sub> to trigger parasitic reactions, where the origin of the parasitic  
23  
24 85 reactions includes the oxidation of the electrolyte and the carbon electrode, consequently  
25  
26 86 forming side products such as carbonates, carboxylates, formates and acetates.<sup>8, 23-25</sup> However,  
27  
28 87 such results were obtained *ex situ*, hence leaving questions concerning the underpinning  
29  
30 88 mechanism or the effect of post-mortem sample handling, open.  
31  
32  
33

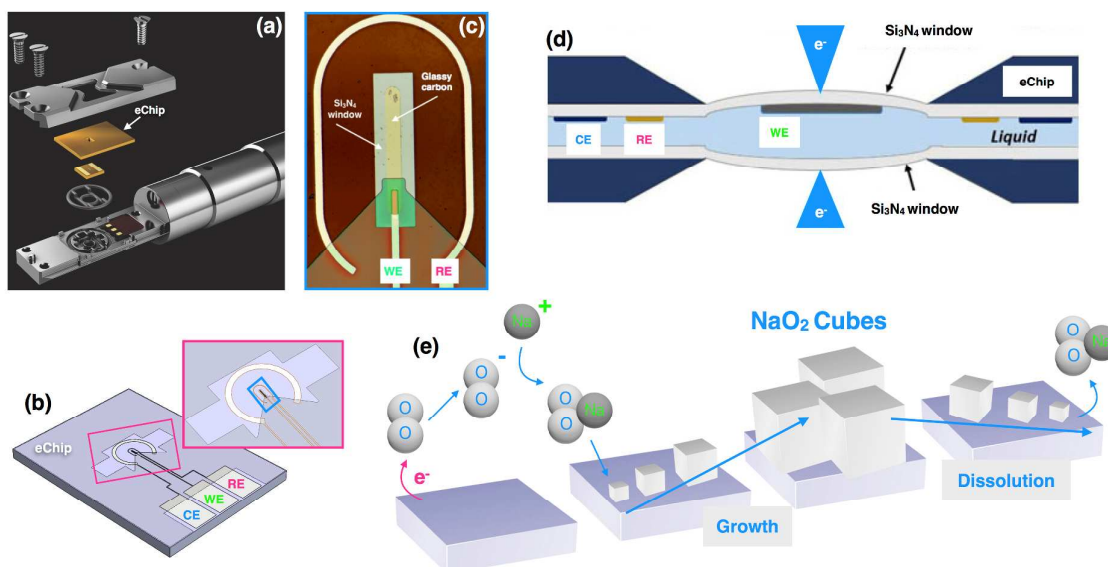
34 89 Altogether, these studies clearly demonstrate the complexity of the Na-O<sub>2</sub> system, which have  
35  
36 90 slowed down its development. Thus, there is a need to move away from the conventional  
37  
38 91 analytical *ex situ* characterization methods and develop *operando* techniques to pin-down  
39  
40 92 fundamental mechanisms in real-time.<sup>26</sup> The recent development of liquid cell for  
41  
42 93 transmission electron microscopy<sup>27</sup> enables an exciting opportunity to explore<sup>28, 29</sup> and even  
43  
44 94 quantify<sup>30-32</sup> complex electrochemical reactions occurring inside batteries during operation. In  
45  
46 95 the present study, we monitor for the first time the discharge and charge reactions occurring in  
47  
48 96 a liquid aprotic Na-O<sub>2</sub> battery by using an *operando* electrochemical (scanning) transmission  
49  
50 97 electron microscopy (STEM and TEM) Na-O<sub>2</sub> micro battery setup coupled with fast imaging.  
51  
52 98 This setup enables us to unambiguously prove that not only does the growth occur by a  
53  
54 99 solution-mediated processes in glyme-ether electrolytes, but so does the oxidation of NaO<sub>2</sub>  
55  
56  
57  
58  
59  
60

1  
2  
3 100 cubes. Further, we visualize the formation of side products leading to the formation of  
4  
5 101 parasitic shell at the interface between NaO<sub>2</sub> crystals and the electrolyte, which remains as  
6  
7 102 solid residues on the electrode after charge.

### 9 103 **Benchmarking the Na-O<sub>2</sub> micro-battery setup**

10  
11  
12 104 Figure 1 shows a schematic of the micro-battery based on the electrochemical TEM cell  
13  
14 105 configuration (a-d) used throughout this work for the *operando* imaging of sub-micrometric  
15  
16 106 features during redox reactions at the positive carbon electrode (e). The *operando* cell was  
17  
18 107 assembled using an oxygen-saturated electrolyte made of 0.5M NaPF<sub>6</sub> dissolved into  
19  
20 108 monoglyme (DME), which contains < 20 ppm of water as determined by Karl-Fischer  
21  
22 109 titration. To establish its electrochemical performance, the *operando* cell was charged and  
23  
24 110 discharged in a cyclic-voltammetry mode, using a sweep rate of 10 mV/s between and Pt as  
25  
26 111 counter and pseudo-reference electrodes (Supplementary Figure S1). Such conditions were  
27  
28 112 used due to the extremely small size of the cell setup, restricting the volume of the electrolyte  
29  
30 113 as well as the available amount of dissolved O<sub>2</sub>. We first verified that these conditions provide  
31  
32 114 similar results as classical Swagelok cells, with namely the formation of discharge products  
33  
34 115 consisting of plentiful cubes (Figure 2a and 2b), which were identified as NaO<sub>2</sub> by combining  
35  
36 116 energy dispersive X-ray spectroscopy (EDX) and selected area electron diffraction (SAED) as  
37  
38  
39  
40 117 discussed later in greater detail.

118



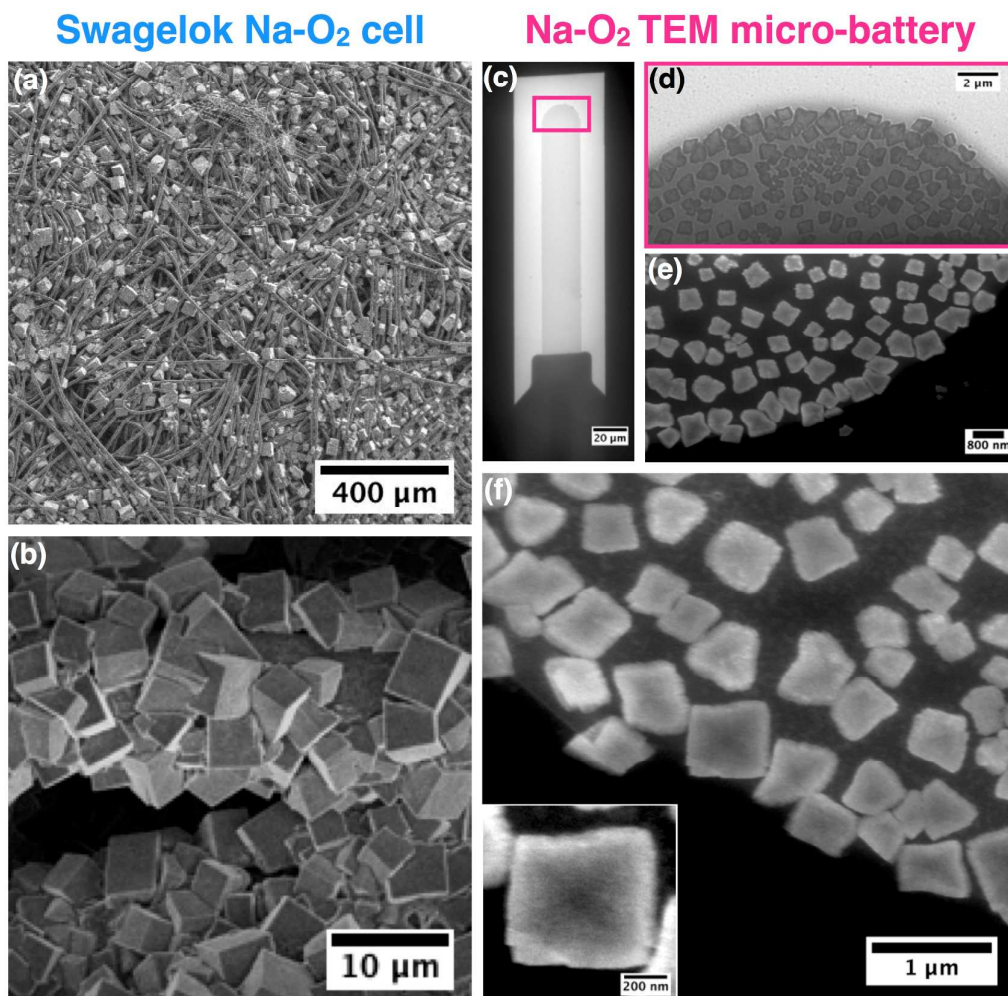
119

120 **Figure 1:** Schematic description of the Poseidon 510 TEM holder for *operando*  
 121 electrochemical measurements: exploded view showing the holder tip with precision slot for  
 122 loading liquid cell (a), where the top e-chip containing a printed reference (platinum), counter  
 123 (platinum) and working electrode (glassy carbon) (b, c) is mounted on top of the bottom e-  
 124 chip containing an electron beam transparent  $\text{Si}_3\text{N}_4$  membrane, O-rings gasket is used to get a  
 125 good vacuum-sealing. Cross-sectional illustration of the *operando* electrochemical TEM cell  
 126 with the pathway of the electron beam and thin conductive glassy carbon electrode (d).  
 127 Schematic of the electrochemically induced discharge and charge processes, taking place at  
 128 the positive electrode surface (e).

129

130 Equally, the inhomogeneous dispersion in size and morphology for the cubes obtained on the  
 131 glassy carbon electrode (GC) in the *operando* cell (loaded with liquid electrolyte) Figure 2d -  
 132 f, compares well with  $\text{NaO}_2$  cubes found in Swagelok-cells on carbon fibers (Figure 2a and  
 133 2f).<sup>33, 34</sup> Nevertheless, smaller  $\text{NaO}_2$  cubes are formed with the *operando* TEM cell (0.5 - 1  
 134  $\mu\text{m}$ ) that is explained by the geometry of the cell, *i.e.* the reduced distance between the two

1  
2  
3 135  $\text{Si}_3\text{N}_4$  windows, which limits the amount of electrolyte and thus  $\text{O}_2$ , as well as the short  
4  
5 136 discharge period during CV.  
6  
7



138 **Figure 2:** Comparison of Na-O<sub>2</sub> morphology obtained in regular Na-O<sub>2</sub> Swagelok cells on  
139 carbon fibers (Freudenberg gas diffusion layer electrodes) (a-b) and the GC electrodes used in  
140 the Na-O<sub>2</sub> TEM micro-battery setup (c-f), (images a-d, taken after removal of the electrolyte).  
141 The SEM overview image of the carbon fibers shows the dense coverage by NaO<sub>2</sub> discharge  
142 product (a) and the high magnification SEM image depicts the micrometer-sized cubic  
143 morphology found in Swagelok cells (b). Low magnification TEM image of the GC working  
144 electrode used in the *in situ* Na-O<sub>2</sub> micro-battery cell (c). TEM and HAADF-STEM overview  
145 images in presence of liquid electrolyte showing, similar to Swagelok cells, NaO<sub>2</sub> cubes



1  
2  
3 146 covering the GC electrode after discharge (anodic CV scan, 10 mV/s) (d, e). The enlarged  
4  
5 147 HAADF-STEM images illustrate the inhomogeneous NaO<sub>2</sub> cubes morphology (f and insert);  
6  
7 148 where the thick layer of liquid electrolyte about 1 μm between the electrode surface and the  
8  
9 149 bottom silicon nitride window impacts the image quality even in HAADF-STEM mode.  
10  
11  
12 150

### 151 **Visualizing the growth process of NaO<sub>2</sub> during discharge**

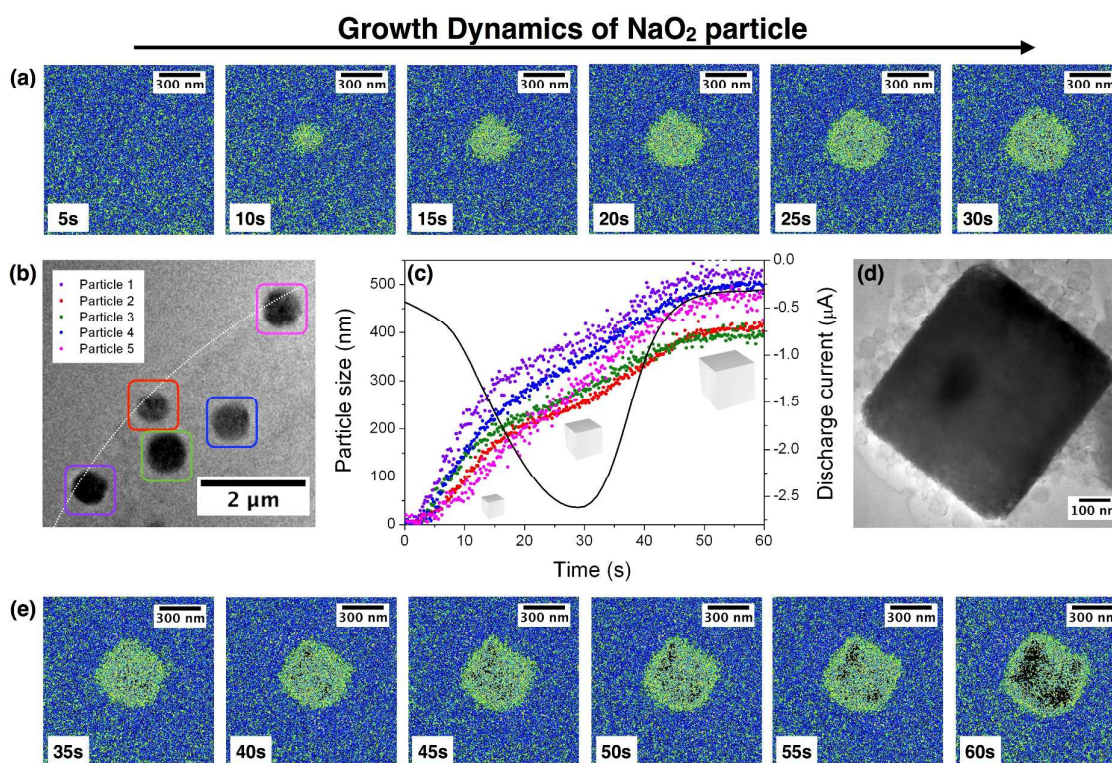
152 The growth of NaO<sub>2</sub> cubes during discharge was followed by means of fast TEM imaging  
153 and high angle annular dark field STEM (HAADF-STEM) using the same cycling conditions  
154 as previously mentioned (Figure 3, sequence a and e, Supplementary Video S1). Comparing  
155 the electrochemical response in Figure 3 c with the image sequence in Figure 3 a shows that  
156 the cube growth follows a solution-precipitation mechanism. Indeed, after an initial step  
157 where the electrolyte is saturated by the electrochemically produced NaO<sub>2</sub> soluble species  
158 (image at 5 s, cathodic current in CV of Figure S1), a point of super saturation is then reached  
159 as characterized by the formation of small NaO<sub>2</sub> nuclei on the electrode surface (image at 10  
160 s). This initial incubation period, where cathodic current corresponding to the electrochemical  
161 formation of soluble NaO<sub>2</sub> is measured but no product is formed on the electrode, is  
162 characteristic of a crystal growth following a solution-precipitation mechanism and therefore  
163 rules out a surface-directed growth of NaO<sub>2</sub> cubes, for which NaO<sub>2</sub> would grow as a solid  
164 following the cathodic current. Such nuclei subsequently grow in an isotropic manner (images  
165 at 15 - 60 s), by deposition of solvated NaO<sub>2</sub> on the surface of cubes. This growth ultimately  
166 leads to the formation of NaO<sub>2</sub> cubes with a size of approx. 500 nm (image at 60 s). Hence,  
167 three stages for the solution-mediated cube-growth precipitation process, similar to the first  
168 description given by Janek and coworkers,<sup>15</sup> could be spotted. First, soluble NaO<sub>2</sub> is  
169 electrochemically formed and quickly saturate the electrolyte (owing from the low solubility

1  
2  
3 170 of NaO<sub>2</sub> in organic solvents)<sup>15, 34</sup>. Once supersaturation of the electrolyte is reached, small  
4  
5 171 aggregates of solvated (NaO<sub>2</sub>)<sub>n</sub> species precipitate in the form of small NaO<sub>2</sub> nuclei on the  
6  
7 172 carbon electrode. Finally, upon discharge, soluble NaO<sub>2</sub> species are consistently produced and  
8  
9 173 deposit on the high surface energy nuclei, which ultimately grow into larger NaO<sub>2</sub> cubes. We  
10  
11 174 would like to emphasize here is that the electrode surface in Figure 3 sequence a and e, is hard  
12  
13 175 to visualize owing to the thick layer of electrolyte between the electrode and the Si<sub>3</sub>N<sub>4</sub>  
14  
15 176 window. Hence, to facilitate its identification, a thin white line is used, as a guide to the  
16  
17 177 reader, to indicate the electrode border in TEM image in Figure 3 b.  
18  
19

20  
21 178

22  
23 179 Further exploiting the capability of the TEM setup, we visualize the sequential size evolution  
24  
25 180 of several cubes (Figure 3 b, supplementary Video S2). As NaO<sub>2</sub> is an insulator<sup>15, 16</sup> and  
26  
27 181 cannot grow by electrodeposition, it is evident that the gradual growth occurs by deposition of  
28  
29 182 NaO<sub>2</sub> from the solution at the outer crystal surface. For better quantification, the particle size  
30  
31 183 evolution during discharge as a function of the growth time was plotted, which revealed the  
32  
33 184 non-linear intermittent growth rate (Figure 3 c). Initially, the electrolyte is being saturated  
34  
35 185 with electrochemically generated NaO<sub>2</sub> and no significant deposit can be observed. Once the  
36  
37 186 saturation limit is reached, a rapid increase of the cube size is observed, which could be  
38  
39 187 associated with the large concentration of NaO<sub>2(solv)</sub> in solution at the point of super  
40  
41 188 saturation. This initial burst is then followed by step-wise regime associated with domains of  
42  
43 189 low and high growth rates, dependent on the local concentration of NaO<sub>2</sub> in solution. Lastly, a  
44  
45 190 steady-state regime is reached towards the end of discharge where the growth rate diminishes  
46  
47 191 due to depletion of O<sub>2</sub> in the electrolyte, causing the limited current density as recorded by  
48  
49 192 CV (Figure 3 c). By analyzing several cubes, we could demonstrate that the overall  
50  
51 193 mechanism is similar for every cube, verifying the ubiquitous nature of this process with,  
52  
53 194 however, different intermittent growth rates for each cube, thus further pointing out the  
54  
55  
56  
57  
58  
59  
60

195 important role played by the mass transport, owing to the different local environment (*i.e.* the  
 196 density of neighboring cubes) (Figure 3 c). To the best of our knowledge, this is the first  
 197 acquisition of such insights regarding the solution-mediated growth of NaO<sub>2</sub>. These results,  
 198 combined with the previously demonstrated solubility of NaO<sub>2</sub><sup>15, 34</sup> unambiguously establish  
 199 that the insulating NaO<sub>2</sub> phase<sup>15, 16</sup> formed during discharge of a Na-O<sub>2</sub> battery is the  
 200 consequence of a solution-mediated precipitation process.



202

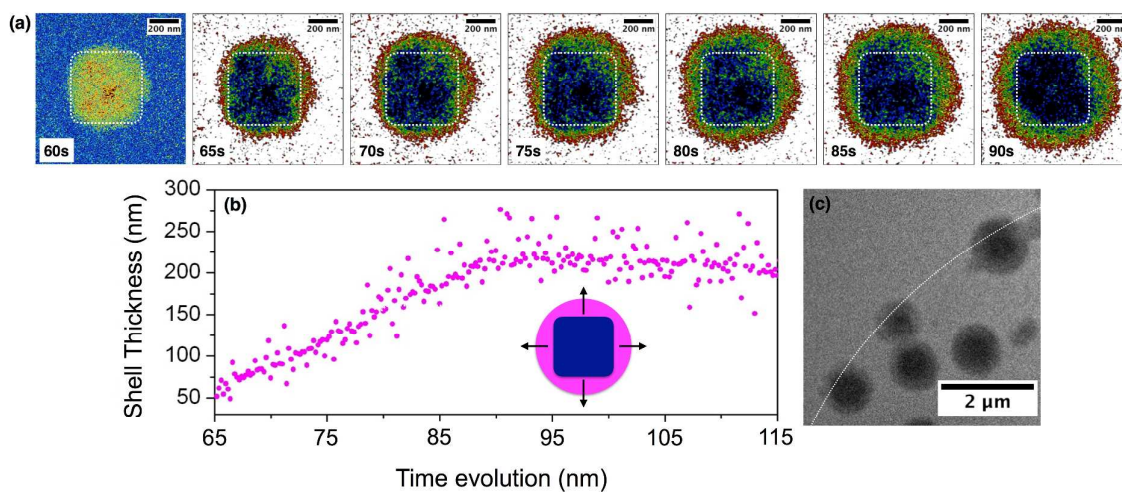
203 **Figure 3:** The time-resolved and animated *operando* TEM images illustrate the  
 204 morphological evolution of the NaO<sub>2</sub> product during discharge (a and e), featuring a  
 205 nucleation event (10 s) and the subsequent growth of NaO<sub>2</sub> cubes, following a solution-  
 206 mediated growth-process (11-60 s). TEM image extracted from the growth study of several  
 207 cubes (pink, blue, green, red and black circles in b) forming during discharge. The size-  
 208 evolution analysis of these cubes reveals a non-linear growth with intermittent plateaus  
 209 demonstrating the NaO<sub>2(solv)</sub> diffusion dependency of this process (c). The black line indicates

1  
2  
3 210 the anodic current response obtained during discharge. Enlarged TEM image of a cube  
4  
5 211 obtained at the end of discharge, surrounded by parasitic shell. (d) High-resolution TEM  
6  
7 212 image of NaO<sub>2</sub> cube, obtained on the GC electrode at the end of discharge.  
8

9 213

#### 11 214 **Formation of parasitic shell**

14 215 Quite interestingly, the use of *operando* TEM also enables identification of a shell  
15  
16 216 surrounding the NaO<sub>2</sub> cubes, which becomes predominant towards the end of discharge (>  
17  
18 217 60s) (Figure 4 a, image 65 s – 85s, green and orange pixels). We further exploited the  
19  
20 218 capabilities of *operando* TEM by visualizing the evolution of this shell surrounding the cubic  
21  
22 219 NaO<sub>2</sub> crystal (Supplementary Video S3), shell which is initially appears as a thin film prior to  
23  
24 220 develop into a thick spherical shell (approx. 200 nm) around the cube. Hence, several  
25  
26 221 questions arise from this observation: what is the nature of this shell and what is its  
27  
28 222 consequence for the performance of the Na-O<sub>2</sub> battery?  
29  
30



224 **Figure 4:** The fast and animated *operando* TEM images showing the evolution of the  
225 parasitic shell at the cube-electrolyte interface, illustrated by the orange/green pixels (a). Shell  
226 thickness evolution, extracted from the numerical treatment of image stack after contrast  
227 filtering, indicated in pink, insert (b). TEM image of finally obtained NaO<sub>2</sub> cubes (strong

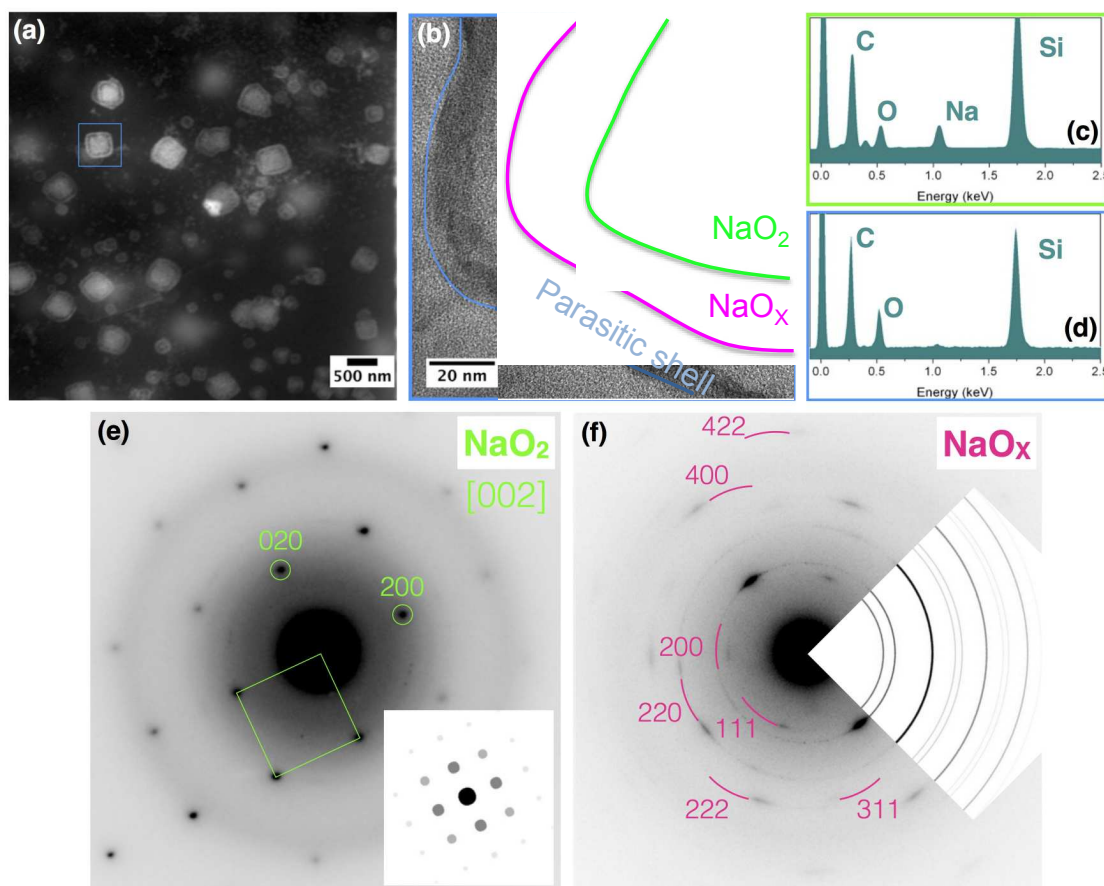
1  
2  
3 228 contrast), surrounded by the parasitic shell (light contrast) (c). Note that cubes are growing on  
4  
5 229 the surface of the glassy carbon electrode, the extremity of which is represented by the white  
6  
7 230 line.

8  
9  
10 231

### 11 12 232 **Analyzing the discharge products**

13  
14  
15 233 By moving to *ex situ* TEM, EDX and SAED analysis, we could provide further insights in  
16  
17 234 both the chemical composition and the morphology of this shell (Figure 5). Note that this  
18  
19 235 shell, which is separated from crystalline NaO<sub>2</sub> cube by a darker line (in the HAADF-STEM  
20  
21 236 mode), can be found on the surface of every cube (Figure 5 a). Furthermore, the use of TEM  
22  
23 237 reveals the presence of three different morphologies and chemical compositions from the bulk  
24  
25 238 to the surface of a cube (Figure 5 b). First, the bulk crystal (green/blue area) was identified to  
26  
27 239 have the composition of Na:O<sub>2</sub> by means of EDX and to crystallize in the fluorite structure of  
28  
29 240 NaO<sub>2</sub> (S.G. Fm-3m) as deduced by SAED (Figure 5 c, e). Moving towards the surface, TEM  
30  
31 241 reveals a first shell growing on the bulk NaO<sub>2</sub> crystal (pink area), which consists of an  
32  
33 242 agglomeration of nano-cubes with crystallite size of about 20 nm. The SAED pattern of the  
34  
35 243 nano-cubes (Figure 5 f) shows rings of modulated intensity confirming the visual observation  
36  
37 244 of numerous randomly oriented crystallites, having a cubic unit cell parameter close to that  
38  
39 245 measured for the SAED pattern of NaO<sub>2</sub>. Although the absolute values for the lattice  
40  
41 246 parameters cannot be precisely measured from SAED patterns, their ratio can be estimated  
42  
43 247 with much higher precision. This estimate gives the  $a_{\text{nano-cubes}}/a_{\text{NaO}_2} \approx 1.015$  value. Both, the  
44  
45 248 fluorite-type NaO<sub>2</sub> and antiferite-type Na<sub>2</sub>O both possess the face-centered cubic unit cell  
46  
47 249 with the cell parameter ratio  $a_{\text{Na}_2\text{O}}/a_{\text{NaO}_2} = 5.56\text{\AA}/5.512\text{\AA} = 1.009$  that is reminiscent to the  
48  
49 250 experimentally measured ratio. Thus, one can tentatively identify the nano-cubes as defective  
50  
51 251 NaO<sub>2</sub>, with an increased Na:O atomic ratio (note that Na<sub>2</sub>O<sub>2</sub> would adopt an hexagonal  
52  
53  
54  
55  
56  
57  
58  
59  
60

1  
2  
3 252 symmetry while  $\text{Na}_2\text{O}_2 \cdot 2\text{H}_2\text{O}$  would adopt a monoclinic symmetry). These high surface area  
4  
5 253 cubes may further favor the chemical reactivity towards electrolyte decomposition as seen by  
6  
7 254 the formation of the third shell, an amorphous layer at the outer surface, *i.e.* at the interface  
8  
9 255 between the cubes and the electrolyte, with reduced Na content as deduced by the small  
10  
11 256 sodium peak observed by EDX analysis (Figure 5 d, blue line). To shine further light on this  
12  
13 257 amorphous outer layer, GDL electrodes were discharged using classical Swagelok cells. The  
14  
15 258 electrodes, which contain large amounts of discharge product, were then analyzed in greater  
16  
17 259 details.



261 **Figure 5:** *Ex situ* analysis (dry condition) of the discharge product. HAADF-STEM overview  
262 image of the widely distributed cubes on the GC electrode, surrounded by the parasitic shell

1  
2  
3 263 (a). TEM image illustrating the interior of the shell around the NaO<sub>2</sub> cubes; bulk crystalline  
4  
5 264 NaO<sub>2</sub> (green), NaO<sub>x</sub> nanocrystalites (pink) and the outer organic layer (blue) (b). EDX spectra  
6  
7 265 of the NaO<sub>2</sub> bulk (c) and the organic layer (d). SAED patterns showing the high crystallinity  
8  
9 266 of inner NaO<sub>2</sub> bulk (e) and poly-dispersed NaO<sub>x</sub> nanocrystalites for the second layer (f).

10  
11  
12 267

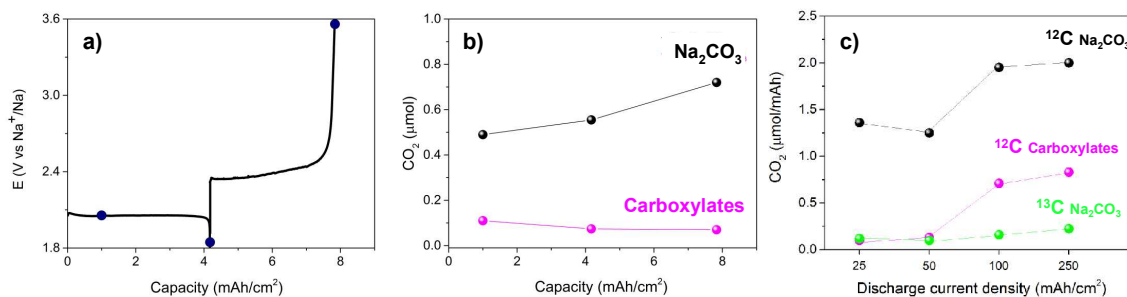
13  
14  
15 268 First, HAADF-STEM analysis of discharged GDL electrodes revealed the presence of a shell  
16  
17 269 for NaO<sub>2</sub> cubes grown in classical Swagelok cells, similarly to what was observed using the in  
18  
19 270 situ TEM setup (Supplementary Figure S6). This validates the observations made by the  
20  
21 271 operando-cell and further exclude beam damage as the sole origin for the formation of this  
22  
23 272 shell.

24  
25  
26 273 To gain deeper understanding about this shell, XPS spectra of discharged GDL electrodes  
27  
28 274 were collected at various stages of discharge (Supplementary Figure S2). The C1s spectra  
29  
30 275 reveal the constant evolution of a parasitic carbonate-like species during discharge. To  
31  
32 276 quantify the amount of these carbonates generated upon discharge, we relied on the method  
33  
34 277 first described by Thotiyl et al.<sup>35</sup> that consist in the use of acid (H<sub>3</sub>PO<sub>4</sub>) and Fentons's reagent  
35  
36 278 are used to decompose inorganic and organic carbonates, with the CO<sub>2</sub> generated through  
37  
38 279 their decomposition being subsequently sampled by a mass spectrometer.

39  
40  
41  
42 280 The released CO<sub>2</sub> concentration at various stages of discharge (Figure 6) indirectly,  
43  
44 281 demonstrates the significant amount of inorganic Na<sub>2</sub>CO<sub>3</sub> and organic carboxylates formed on  
45  
46 282 the surface of carbon electrodes. Upon discharge, the concentration of inorganic carbonates  
47  
48 283 significantly increases (Figure 6 b), and this is in agreement with the growth of the shell  
49  
50 284 observed in Figure 4a. Moreover, when comparing the concentration of Na<sub>2</sub>CO<sub>3</sub> at the end of  
51  
52 285 discharge with the results obtained at the end of charge, a limited increase is found for GDL  
53  
54 286 electrodes, demonstrating that the parasitic products cannot be reoxidized and remain on the

287 electrode surface at the end of charge (Figure 6b). This result highlights the importance of  
 288 mastering this interface for decreasing the rate of parasitic product formation.

289



290

291 **Figure 6:** Discharge–charge profiles for GDL electrode at a rate of  $25 \mu\text{A}/\text{cm}^2$  (a). Amount  
 292 of  $\text{CO}_2$  evolved from the GDL electrode when removed from the cells at different states of  
 293 discharge and charge and treated with acid and Fenton’s reagent to decompose  $\text{Na}_2\text{CO}_3$  and  
 294 organic carboxylates (b).  $\text{CO}_2$  evolution originating from the instability of electrode and  
 295 electrolyte as deduced from the discharge of  $^{13}\text{C}$ -carbon electrodes at various discharge rates  
 296 between  $25 - 250 \mu\text{A}/\text{cm}^2$  (c).  $^{12}\text{C}$  evolution indicates the electrolyte degradation leading to  
 297 inorganic carbonates (black) and organic carboxylates (red) whereas  $^{13}\text{C}$  detection results  
 298 from the direct decomposition of the carbon electrodes.

299

300 Finally, to clarify the origin of the carbonate side product formation, which can result from  
 301 the electrolyte and/or from the electrode decomposition, discharge experiments using  $^{13}\text{C}$ -  
 302 labeled electrodes with the released  $\text{CO}_2$  isotopes being detected by mass Spectrometry  
 303 analysis. These isotopic experiments revealed the presence of both  $^{13}\text{CO}_2$  and  $^{12}\text{CO}_2$  at the end  
 304 of discharge, which can only be explained by the decomposition of both the electrode surface  
 305 and the electrolyte, respectively (Figure 6c). However, the observed  $^{12}\text{C}$  fraction was much  
 306 larger than the  $^{13}\text{C}$  one, demonstrating that the majority of parasitic carbonates originates from



1  
2  
3 307 the instability of the glyme-electrolyte in contact with the highly oxidizing NaO<sub>2</sub> discharge  
4  
5 308 product. Again, this result corroborates the shell formation we observed in Figure 4.  
6  
7 309 Additionally, we observed that upon elevated discharge currents, the amount of products  
8  
9 310 originating from the decomposition reactions increases, with a prominent contribution from  
10  
11 311 the electrode decomposition (Figure 6c), hence implying that an electrochemically-driven-  
12  
13 312 electrode decomposition is also at play during discharge of Na-O<sub>2</sub> batteries.

14  
15  
16 313 Altogether, these experiments reveal the high reactivity of NaO<sub>2</sub> and further disproves,  
17  
18 314 together with previous literature reports,<sup>8, 23-25</sup> the initial claim of improved stability for Na-  
19  
20 315 O<sub>2</sub> batteries when compared to Li-O<sub>2</sub> ones.<sup>5</sup>

21  
22  
23 316

24  
25  
26 317 Overall, the combination of the time-resolved TEM as well as *ex situ* observations reveal that  
27  
28 318 parasitic reactions in glyme-ether based Na-O<sub>2</sub> batteries constantly occur during discharge,  
29  
30 319 demonstrating the strong reactivity of NaO<sub>2</sub> towards the electrolyte and potentially residual  
31  
32 320 impurities such as *e.g.*: H<sub>2</sub>O or CO<sub>2</sub><sup>18, 20, 21</sup> or even the generation of singlet O<sub>2</sub> species, as  
33  
34 321 recently reported for Li-O<sub>2</sub> and Na-O<sub>2</sub> batteries.<sup>36-38</sup> At this stage, it is worth noting that the  
35  
36 322 carbonates are certainly not the only one kind of parasitic products formed when cycling Na-  
37  
38 323 O<sub>2</sub> batteries. Indeed, several very recent reports demonstrated the high reactivity of NaO<sub>2</sub>  
39  
40 324 towards the electrode, as well as towards the solvent,<sup>8, 23, 24</sup> where sodium carbonate and  
41  
42 325 carboxylate were identified to be the main parasitic products, with a variety of other side  
43  
44 326 products, such as formates and acetates also being found.

45  
46  
47  
48 327

49  
50  
51 328 Overall, we believe that preventing the formation of this complex organic/inorganic shell will  
52  
53 329 be of prime importance to mitigate the drastic capacity loss observed upon cycling with  
54  
55 330 today's Na-O<sub>2</sub> cells, which will be discussed in greater details below.

1  
2  
3 331 **Resolving the mechanism in charge – the dissolution of NaO<sub>2</sub>**

4  
5 332 Encouraged by the mechanistic insight provided by *operando* TEM during the discharge of  
6  
7 333 Na-O<sub>2</sub> battery, we decided to explore the oxidation process following the same methodology.  
8  
9 334 From a sequence of images collected by HAADF-STEM (Supplementary Video S4), the  
10  
11 335 gradual dissolution of NaO<sub>2</sub> cubes during oxidation can be observed (Figure 7). More  
12  
13 336 importantly, this visualization shows that cubes dissolve concentrically from the outside  
14  
15 337 inwards. In detail, the 3D visualization of the processes at play during charge illustrate that  
16  
17 338 the dissolution of the cubes initially proceeds from the top surface, *i.e.* at the interface  
18  
19 339 between the cube and the electrolyte, leading to a steady decrease in size of the cube (Figure 7  
20  
21 340 a-d). This is in contrast to the previously reported electrode directed charge-transfer, *i.e.* the  
22  
23 341 direct oxidation of the cubes at the interface with the electrode.<sup>12</sup> To gain deeper insight into  
24  
25 342 this dissolution process, the height-profile evolution was followed for one cube throughout  
26  
27 343 the complete oxidation (Figure 7 e-h). From this profile, it can be observed that cubes, despite  
28  
29 344 being covered by the parasitic shell, start to dissolve from the top, *i.e.* the face exposed to the  
30  
31 345 electrolyte, hence demonstrating the porous nature of the organic shell. Upon further  
32  
33 346 charging, the overall height profile continuously decreases from the top of the cube, further  
34  
35 347 suggesting a collapse of the parasitic shell during charge. Ultimately, parts of the shell remain  
36  
37 348 at the end of charge spread on the surface of the electrode, visualized in Figure 7 i as a  
38  
39 349 patchwork and by the “walls” at 50 and 300 nm in the linear profile in Figure 7 h. This is in  
40  
41 350 good agreement with our *ex situ* observations where parasitic residues (organic and inorganic)  
42  
43 351 are found on the GDL carbon fibers after charge (Figure 6), as well as with previous reports.<sup>8</sup>  
44  
45 352 Altogether, these new information shine light on a so-far poorly explained phenomenon,  
46  
47 353 namely the constant columbic losses measured upon cycling. Subsequent cycling will indeed  
48  
49 354 generate additional parasitic products that will accumulate at the electrode surface, ultimately  
50  
51 355 causing a rapid capacity loss and a drastic self-discharge.  
52  
53  
54  
55  
56  
57  
58  
59  
60

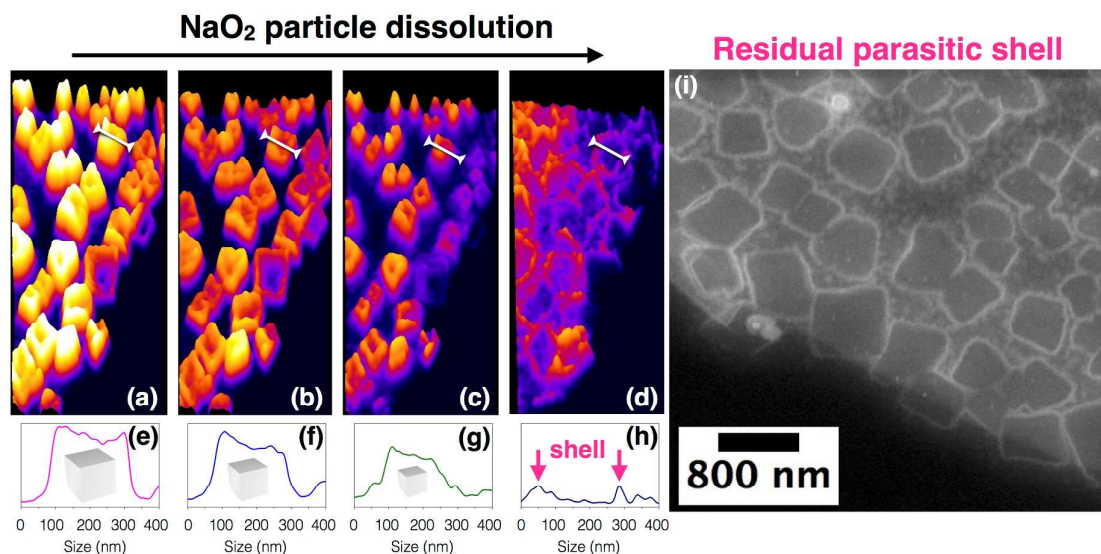
356

357 In light of the solvation-desolvation equilibrium discussed above, our *operando* electron  
358 microscopy measurements provide the definitive demonstration that the oxidation process in  
359 Na-O<sub>2</sub> batteries follows a solution-mediated mechanism, as previously proposed<sup>15</sup> based on  
360 the significant solubility of NaO<sub>2</sub>,<sup>15, 34</sup> its low dissolution energy<sup>10, 13</sup> as well as its insulating  
361 nature that would prohibit direct oxidation at the electrode.<sup>15, 16</sup> During charge, solvated  
362 NaO<sub>2(solv)</sub> is oxidized at the electrode surface into Na<sup>+</sup> and O<sub>2(g)</sub>, hence displacing the  
363 equilibrium NaO<sub>2(solid)</sub> = NaO<sub>2(solv)</sub> to the right and forcing the dissolution of the cubes.  
364 Through this process, the bottom edges of the non-conducting cubes, in direct contact with the  
365 electrode surface, remain throughout the charge as evidenced by TEM. This clearly contrasts  
366 with the previously proposed mechanism for which a direct charge transfer between the solid  
367 and the electrode/current collector was a requirement.<sup>12</sup>

368

369 Finally, we explored the consequences of the formation of parasitic products at the electrode  
370 surface on subsequent cycles and NaO<sub>2</sub> formation. This revealed that NaO<sub>2</sub> nuclei were  
371 exclusively formed during the second discharge on the uncovered, pristine electrode surface  
372 (Supplementary Video S5). Hence, the parasitic products not only hamper the O<sub>2(g)</sub> redox  
373 reaction but also hinder NaO<sub>2</sub> nucleation on the carbon surface. In short, this study shows that  
374 the formation of parasitic products has its origin in the high chemical reactivity of the NaO<sub>2</sub>  
375 cube surface, initially suspected to be less reactive than Li<sub>2</sub>O<sub>2</sub>.<sup>5</sup> This highlights the need for a  
376 new class of electrolytes that are stable against attack from NaO<sub>2</sub>.

377



378

379 **Figure 7:** HAADF-STEM imaging of the charge process. Animated images at different depth  
 380 of charge depict the dissolution of the cubes via solution, starting at cube-electrolyte interface  
 381 and proceeding downwards to the electrode surface (a-d). High profile evolution of a single  
 382 cube during charge (specified by white bar in a-d) (e-h) further supporting the solution-  
 383 mediated charge, where the two bumps at 50 and 300 nm in image h indicate the parasitic  
 384 shell remaining on the electrode surface at the end of the charge. HAADF-STEM image of the  
 385 GC electrode surface after discharge showing the patchwork of the residual parasitic shells,  
 386 blocking subsequent O<sub>2</sub> redox and NaO<sub>2</sub> nucleation (i).

387

### 388 Conclusion

389 Herein we have reported that fast imaging TEM and HAADF-STEM are powerful  
 390 analytical tools to understand the mechanistic pertaining to the charge/discharge processes in  
 391 DME based Na-O<sub>2</sub> batteries. We visualized the solution-mediated growth of NaO<sub>2</sub> in real-  
 392 time and identified that the 3D growth process is governed by the equilibrium between  
 393 NaO<sub>2(solv)</sub> <--> NaO<sub>2(solid)</sub> and the mass transport of soluble product. By imaging the charge

1  
2  
3 394 process, we provide conclusive evidence that the same solvation-desolvation equilibrium is  
4  
5 395 responsible for the dissolution of the NaO<sub>2</sub> discharge product, which consumes the NaO<sub>2</sub>  
6  
7 396 cubes from the NaO<sub>2</sub>-electrolyte interface towards the electrode and not from the cube-  
8  
9 397 electrode interface. Therefore, we rule out the direct charge-transfer reaction as the major  
10  
11 398 oxidation path for NaO<sub>2</sub> cubes and clarify the mechanism of this widely discussed reaction.  
12  
13 399 Finally, we provide fundamental insights into the parasitic reactions occurring during cycling  
14  
15 400 of a Na-O<sub>2</sub> battery where time-resolved visualization revealed the chemical reactivity of NaO<sub>2</sub>  
16  
17 401 at the interface with the electrolyte. As a result, parasitic products continuously accumulate on  
18  
19 402 the cube surface to form a thick shell surrounding the NaO<sub>2</sub> cubes, which passivates the  
20  
21 403 electrode surface as it cannot be reoxidized. This information is vital for optimization of the  
22  
23 404 battery, since this parasitic shell is responsible for the low efficiency during charge, as well as  
24  
25 405 for its poor cyclability by preventing crucial O<sub>2</sub> redox and further nucleation of NaO<sub>2</sub>. It must  
26  
27 406 therefore be recognized that the NaO<sub>2</sub> growth is solvent dependent, providing the possibility  
28  
29 407 of mediating the deposition process by controlling the solvation/desolvation event. Hence,  
30  
31 408 caution must be exercised prior to generalizing this finding. Through this first visualization of  
32  
33 409 the redox processes governing the Na-O<sub>2</sub> system, we further confirm the importance of  
34  
35 410 finding how the various components of the batteries locally interact with each other. We hope  
36  
37 411 these results will help in the development of new strategies to optimize cell components, such  
38  
39 412 as the electrolyte, in order to achieve high performing Na-O<sub>2</sub> batteries, and also serve to  
40  
41 413 motivate the development of *operando* electrochemical TEM cells.  
42  
43  
44  
45  
46  
47  
48

414

## 415 **Methods**

### 416 ***Electrolyte preparation:***

417 1,2-Dimethoxyethane (DME, 99.9%) was purchased from Sigma Aldrich and (NaPF<sub>6</sub> 99.9 %)   
418 was bought from Stella Chemifa. Solvents were dried by means of molecular sieves for 5 days

1  
2  
3 419 to remove excess water and Sodium salts were dried under vacuum at 80°C for 24 hours. The  
4 420 0.5 M electrolyte solutions were prepared in an argon-filled glove box (0.1 ppm O<sub>2</sub>/0.1 ppm  
5 421 H<sub>2</sub>O). The water content of the electrolyte solutions was analyzed by Karl Fischer titration  
6 422 and was found to be below 20 ppm. The electrolyte was saturated with ultrapure O<sub>2</sub>, prior to  
7 423 use in the *in situ* TEM cell.

8  
9  
10  
11 424

### 12 425 ***Operando electrochemical (S)TEM experiments:***

13  
14  
15 426 *Operando* TEM experiments were performed using a FEI-TECNAI G2 (S)TEM equipped  
16 427 with a Schottky field-emission gun and an fast camera Oneview-Gatan (30 fps at 4k). For  
17 428 these experiments the microscope was operated at 200 kV in both conventional TEM and  
18 429 HAADF-STEM modes. In this study, we checked the effect of the electron beam used to  
19 430 make the observations in TEM and STEM modes to be sure that the beam does not have any  
20 431 effect on our results. During the observations, the dose was kept below 10 e<sup>-</sup>/nm<sup>2</sup>s in order to  
21 432 limit beam damage effects. By this way, typical beam effects (bubble and precipitate  
22 433 formations) due to the degradation of the electrolyte by radiolysis effect are avoided. As  
23 434 shown in Supplementary Figure S3, the insignificant impact of the electron beam on the  
24 435 liquid electrolyte was verified with the same dose of electron used during the fast imaging  
25 436 acquisition, which shows a high stability of NaPF<sub>6</sub>/DME/O<sub>2</sub> electrolyte upon electron beam  
26 437 irradiation for a relatively long period of time: 360s. The TEM holder used is a Protochips  
27 438 Poseidon 510 owing both a microfluidic flow system and an electrochemical measurement  
28 439 system with 3 electrodes. The micro-battery cell itself is localized in the holder tip and  
29 440 consists of two silicon Echips sealed by Viton O-ring gasket: a top Echip (with 2 Pt electrodes  
30 441 (reference and counter) and 1 glassy carbon electrodes (working), a 500 nm SU-8 polymer  
31 442 spacer and a 50 nm thick Si<sub>3</sub>N<sub>4</sub> window) and bottom Echip (with a 500 nm spacer and a 50  
32 443 nm thick Si<sub>3</sub>N<sub>4</sub> window). Mounted Echips are then compressed onto O-rings using screwed  
33 444 lid of the holder inducing a good vacuum-sealing. The microfluidic system integrated in the  
34 445 TEM holder allows to introduce and flow the electrolyte with a rate range from 0.5 to 5  
35 446 μL/min. using a syringe pump system. The microfluidic system (cell and microtubes) is  
36 447 flushed by argon gas to discard oxygen presence prior to start *operando* experiment.

37  
38  
39  
40  
41  
42  
43  
44  
45  
46  
47  
48  
49  
50  
51 448

### 52 53 54 449 ***Cyclic voltammetry***

55  
56  
57  
58  
59  
60

1  
2  
3 450 CV experiments were conducted using an ultra low current SP-200 Biologic potentiostat,  
4 451 where during battery cycling, the potential was scanned at a rate of 10 mV/s between -1.6V  
5 452 and -3 V using Pt as pseudo-reference electrode and Pt as counter electrode. For sake of  
6 453 clarity, all values were then rescaled versus  $\text{Na}^+/\text{Na}$  to yield a potential window of 1.5 and  
7 454 2.9V (vs.  $\text{Na}^+/\text{Na}$ ).  
8  
9  
10

11 455

12  
13  
14 456 ***X-ray photoelectron spectroscopy (XPS) analysis:***

15  
16 457 XPS analysis of the surface of aged sodium samples was performed by a means of SPECS  
17 458 Sage HR 100 spectrometer with a non-monochromatic X-ray source (Aluminum  $\text{K}\alpha$  line of  
18 459 1486.6 eV energy and 300 W). The samples were placed perpendicular to the analyzer axis  
19 460 and calibrated using the  $3d_{5/2}$  line of Ag with a full width at half maximum (FWHM) of  
20 461 1.1 eV. All samples were transferred by means of a gastight transfer chamber to avoid air  
21 462 contact. All samples were further rinsed with dry DME solution to remove excess salt. In the  
22 463 case of sodium aged in TFSi electrolyte, the surface of the sample and not the precipitate was  
23 464 analyzed.  
24  
25  
26  
27  
28

29 465 The selected resolution for the spectra was 10 eV of Pass Energy and 0.15 eV/step. All  
30 466 Measurements were made in an ultra-high vacuum (UHV) chamber at a pressure around  
31 467  $5 \cdot 10^{-8}$  mbar. An electron flood gun was used to compensate for charging during XPS data  
32 468 acquisition. In the fittings asymmetric and Gaussian-Lorentzian functions were used (after a  
33 469 Shirley background correction) where the FWHM of all the peaks were constrained while the  
34 470 peak positions and areas were set free. For every anion, XPS was performed on the surface of  
35 471 the metallic sodium. For TFSI, the XPS spectrum was collected as well on the surface of the  
36 472 metallic sodium, while the pilled off part wasn't analyzed.  
37  
38  
39  
40  
41  
42

43 473

44  
45 474 ***Mass Spectrometry analysis:***

46  
47 475 The collected electrodes were first immersed in an aqueous solution containing 2M  $\text{H}_3\text{PO}_4$ ,  
48 476 which decomposes  $\text{Na}_2\text{CO}_3$  into  $\text{CO}_2$ . Due to the very acidic pH-value, the  $2\text{H}^+ + \text{CO}_3^{2-} \leftrightarrow$   
49 477  $\text{HCO}^- + \text{H}^+ \leftrightarrow \text{CO}_2 + \text{H}_2\text{O}$  equilibrium is fully shifted to the right, where  $\text{CO}_2$  evolves as  
50 478 gaseous  $\text{CO}_2$ , which is subsequently sampled by mass spectrometry. In a second step, after the  
51 479  $\text{CO}_2$  evolution has ended and all inorganic  $\text{Na}_2\text{CO}_3$  was quantify, a second injection with 0.5  
52 480 ml of a 2M  $\text{H}_3\text{PO}_4$  solution containing 0.5M  $\text{FeSO}_4$  and 40 $\mu\text{L}$  of 30%  $\text{H}_2\text{O}_2$  (Fenton's  
53  
54  
55  
56  
57  
58  
59  
60

1  
2  
3 481 reagent) was added. The presence of the highly reactive  $\text{OH}^\square$  radical (based on the Fenton's  
4 482 reaction:  $\text{Fe}^{2+} + \text{H}_2\text{O}_2 \rightarrow \text{Fe}^{3+} + \text{OH}^\square + \text{OH}^\square$ ) leads to the decomposition of organic species  
5 483 (e.g.: sodium carboxylates) into  $\text{CO}_2$ , again released as gas due to the acidic environment.  
6  
7  
8  
9

#### 10 11 485 **Author contributions**

12  
13  
14 486 A.G., A.D. and J.-M.T. designed the experiments. L.L., W.D., A.D. and A.G. performed the  
15  
16 487 operando TEM measurements. W.D. and A.D. performed the TEM analysis. L.L., A.G., A.D.  
17  
18 488 and J.-M.T. wrote the manuscript that all the authors edited.  
19  
20

#### 21 489 **Supporting Information Available:**

22  
23  
24 490 Supplementary videos of *in situ* (S)TEM experiments, Cyclovoltammogram, XPS analysis,  
25 491 beam damage control experiments, EELS spectra, STEM-HAADF image, HAADF-STEM  
26 492 and EDX-STEM images of  $\text{NaO}_2$  cubes grown on GDL electrodes.  
27  
28

#### 29 493 **Competing interests**

30  
31  
32 494 The authors declare no competing financial interest.  
33  
34

#### 35 495 **Acknowledgements**

36  
37  
38 496 L.Lutz thanks the ALISTORE-ERI for his Ph.D. grant. We would like to thank Dr. Artem  
39  
40 497 Abakumov for fruitful discussions and comments on the manuscript.  
41  
42

#### 43 498 44 499 **References**

- 45  
46 500 1. Gallagher, K. G.; Goebel, S.; Greszler, T.; Mathias, M.; Oelerich, W.; Eroglu, D.;  
47 501 Srinivasan, V. *Energy & Environmental Science* **2014**, *7*, 1555-1563.  
48 502 2. Bruce, P. G.; Freunberger, S. A.; Hardwick, L. J.; Tarascon, J. M. *Nature Materials*  
49 503 **2012**, *11*, 19-29.  
50 504 3. Abraham, K. M.; Jiang, Z. *J. Electrochem. Soc.* **1996**, *143*, 1-5.  
51 505 4. Lepoivre, F.; Grimaud, A.; Larcher, D.; Tarascon, J.-M. *J. Electrochem. Soc.* **2016**,  
52 506 *163*, A923-A929.  
53 507 5. McCloskey, B. D.; Garcia, J. M.; Luntz, A. C. *J. Phys. Chem. Lett.* **2014**, *5*, 1230-  
54 508 1235.  
55  
56  
57  
58  
59  
60



- 1  
2  
3 509 6. Ottakam Thotiyl, M. M.; Freunberger, S. A.; Peng, Z.; Chen, Y.; Liu, Z.; Bruce, P. G.  
4 510 *Nat Mater* **2013**, 12, 1050-1056.  
5 511 7. Adelhelm, P.; Hartmann, P.; Bender, C. L.; Busche, M.; Eufinger, C.; Janek, J.  
6 512 *Beilstein J. Nanotechnol.* **2015**, 6, 1016-1055.  
7 513 8. Liu, T.; Kim, G.; Casford, M. T. L.; Grey, C. P. *J. Phys. Chem. Lett.* **2016**, 7,  
8 514 4841-4846.  
9 515 9. Bender, C. L.; Hartmann, P.; Vracar, M.; Adelhelm, P.; Janek, J. *Adv. Energy Mater.*  
10 516 **2014**, 4, 1301863.  
11 517 10. Kim, J.; Park, H.; Lee, B.; Seong, W. M.; Lim, H. D.; Bae, Y.; Kim, H.; Kim, W. K.;  
12 518 Ryu, K. H.; Kang, K. *Nat. Commun.* **2016**, 7, 10670-10679.  
13 519 11. Knudsen, K. B.; Nichols, J. E.; Vegge, T.; Luntz, A. C.; McCloskey, B. D.; Hjelm, J.  
14 520 *J. Phys. Chem. C* **2016**, 120, 10799-10805.  
15 521 12. Morasch, R.; Kwabi, D. G.; Tulodziecki, M.; Risch, M.; Zhang, S.; Shao-Horn, Y.  
16 522 *ACS Appl. Mater. Interfaces* **2017**, 9, 4374-4381.  
17 523 13. Lee, B.; Kim, J.; Yoon, G.; Lim, H.-D.; Choi, I.-S.; Kang, K. *Chem. Mater* **2015**, 27,  
18 524 8406-8413.  
19 525 14. Hartmann, P.; Bender, C. L.; Sann, J.; Duerr, A. K.; Jansen, M.; Janek, J.; Adelhelm,  
20 526 P. *Phys. Chem. Chem. Phys.* **2013**, 15, 11661-11672.  
21 527 15. Hartmann, P.; Heinemann, M.; Bender, C. L.; Graf, K.; Baumann, R.-P.; Adelhelm, P.;  
22 528 Heiliger, C.; Janek, J. *J. Phys. Chem. C* **2015**, 119, 22778-22786.  
23 529 16. Yang, S.; Siegel, D. J. *Chem. Mater* **2015**, 27, 3852-3860.  
24 530 17. Xia, C.; Black, R.; Fernandes, R.; Adams, B.; Nazar, L. F. *Nat. Chem* **2015**, 7, 496-  
25 531 501.  
26 532 18. Pinedo, R.; Weber, D. A.; Bergner, B.; Schröder, D.; Adelhelm, P.; Janek, J. *J. Phys.*  
27 533 *Chem. C* **2016**, 120, 8472-8481.  
28 534 19. Ortiz-Vitoriano, N.; Batcho, T. P.; Kwabi, D. G.; Han, B.; Pour, N.; Yao, K. P.;  
29 535 Thompson, C. V.; Shao-Horn, Y. *J. Phys. Chem. Lett.* **2015**, 6, 2636-2643.  
30 536 20. Das, S. K.; Xu, S.; Archer, L. A. *Electrochem. Commun.* **2013**, 27, 59-62.  
31 537 21. Roberts, J. L. J.; Calderwood, T. S.; Sawyer, D. T. *J. Am. Chem. Soc.* **1984**, 106, 4667-  
32 538 4670.  
33 539 22. Sayed, S. Y.; Yao, K. P.; Kwabi, D. G.; Batcho, T. P.; Amanchukwu, C. V.; Feng, S.;  
34 540 Thompson, C. V.; Shao-Horn, Y. *Chem Commun (Camb)* **2016**, 52, 9691-9694.  
35 541 23. Black, R.; Shyamsunder, A.; Adeli, P.; Kundu, D.; Murphy, G. K.; F., N. L.  
36 542 *ChemSusChem* **2016**, 9, 1795 - 1803.  
37 543 24. Landa-Medrano, I.; Pinedo, R.; Bi, X.; Ruiz de Larramendi, I.; Lezama, L.; Janek, J.;  
38 544 Amine, K.; Lu, J.; Rojo, T. *ACS Appl Mater. Interfaces* **2016**, 8, 20120-20127.  
39 545 25. Reeve, Z. E.; Franko, C. J.; Harris, K. J.; Yadegari, H.; Sun, X.; Goward, G. R. *J. Am.*  
40 546 *Chem. Soc.* **2017**, 139, 595-598.  
41 547 26. Liang, Z.; Zou, Q.; Wang, Y.; Lu, Y.-C. *Small Methods* **2017**, 1, 1700150.  
42 548 27. Ross, F. M. *Science* **2015**, 350, aaa9886-aaa9886.  
43 549 28. Dachraoui, W.; Kurkulina, O.; Hadermann, J.; Demortière, A. *Microsc. Microanal.*  
44 550 **2016**, 22, 24-25.  
45 551 29. Holtz, M. E.; Yu, Y.; Gunceler, D.; Gao, J.; Sundararaman, R.; Schwarz, K. A.; Arias,  
46 552 T. A.; Abruna, H. D.; Muller, D. A. *Nano Lett.* **2014**, 14, 1453-1459.  
47 553 30. Mehdi, B. L.; Qian, J.; Nasybulin, E.; Park, C.; Welch, D. A.; Faller, R.; Mehta, H.;  
48 554 Henderson, W. A.; Xu, W.; Wang, C. M.; Evans, J. E.; Liu, J.; Zhang, J. G.; Mueller, K. T.;  
49 555 Browning, N. D. *Nano Lett.* **2015**, 15, 2168-2173.  
50 556 31. Sacci, R. L.; Black, J. M.; Balke, N.; Dudney, N. J.; More, K. L.; Unocic, R. R. *Nano*  
51 557 *Lett.* **2015**, 15, 2011-2018.

- 1  
2  
3 558 32. Luo, L.; Liu, B.; Song, S.; Xu, W.; Zhang, J. G.; Wang, C. *Nat Nanotechnol.* **2017**, *12*,  
4 559 535-540.  
5 560 33. Hartmann, P.; Bender, C. L.; Vracar, M.; Duerr, A. K.; Garsuch, A.; Janek, J.;  
6 561 Adelhelm, P. *Nat. Mater* **2013**, *12*, 228-232.  
7 562 34. Lutz, L.; Yin, W.; Grimaud, A.; Alves Dalla Corte, D.; Tang, M.; Johnson, L.;  
8 563 Azaceta, E.; Sarou-Kanian, V.; Naylor, A. J.; Hamad, S.; Anta, J. A.; Salager, E.; Tena-Zaera,  
9 564 R.; Bruce, P. G.; Tarascon, J. M. *J. Phys. Chem. C* **2016**, *120*, 20068-20076.  
10 565 35. Ottakam Thotiyl, M. M.; Freunberger, S. A.; Peng, Z.; Bruce, P. G. *J. Am. Chem. Soc.*  
11 566 **2013**, *135*, 494-500.  
12 567 36. Wandt, J.; Jakes, P.; Granwehr, J.; Gasteiger, H. A.; Eichel, R. A. *Angew. Chem.* **2016**,  
13 568 *128*, 7006-7009.  
14 569 37. Mahne, N.; Schafzahl, B.; Leypold, C.; Leypold, M.; Grumm, S.; Leitgeb, A.;  
15 570 Strohmeier, G. A.; Wilkening, M.; Fontaine, O.; Kramer, D.; Slugovc, C.; Borisov, S. M.;  
16 571 Freunberger, S. A. *Nat. Energy* **2017**, *2*, 1-9.  
17 572 38. Schafzahl, L.; Mahne, N.; Schafzahl, B.; Wilkening, M.; Slugovc, C.; Borisov, S. M.;  
18 573 Freunberger, S. A. *Angew Chem Int Ed Engl* **2017**, *56*, 15728-15732.

574

575

576

577 **FOR TABLE OF CONTENTS ONLY**

578

